ADVANCED FUNCTIONAL MATERIALS
www.afm-journal.de

Copolymer-Templated Nickel Oxide for High-Efficiency Mesoscopic Perovskite Solar Cells in Inverted Architecture

Faranak Sadegh, Seckin Akin, Majid Moghadam,* Reza Keshavarzi,* Valiollah Mirkhani, Marco A. Ruiz-Preciado, Erdi Akman, Hong Zhang, Mina Amini, Shahram Tangestaninejad, Iraj Mohammadpoor-Baltork, Michael Graetzel, Anders Hagfeldt, and Wolfgang Tress**

Despite the outstanding role of mesoscopic structures on the efficiency and stability of perovskite solar cells (PSCs) in the regular (n–i–p) architecture, mesoscopic PSCs in inverted (p–i–n) architecture have rarely been reported. Herein, an efficient and stable mesoscopic NiO_x (mp-NiO_x) scaffold formed via a simple and low-cost triblock copolymer template-assisted strategy is employed, and this mp-NiO_x film is utilized as a hole transport layer (HTL) in PSCs, for the first time. Promisingly, this approach allows the fabrication of homogenous, crack-free, and robust 150 nm thick mp-NiO_x HTLs through a facile chemical approach. Such a high-quality templated mp-NiO_x structure promotes the growth of the perovskite film yielding better surface coverage and enlarged grains. These desired structural and morphological features effectively translate into improved charge extraction, accelerated charge transportation, and suppressed trap-assisted recombination. Ultimately, a considerable efficiency of 20.2% is achieved with negligible hysteresis which is among the highest efficiencies for mp-NiO_x based inverted PSCs so far. Moreover, mesoscopic devices indicate higher long-term stability under ambient conditions compared to planar devices. Overall, these results may set new benchmarks in terms of performance for mesoscopic inverted PSCs employing templated mp-NiO_x films as highly efficient, stable, and easy fabricated HTLs.

1. Introduction

Hybrid organic-inorganic lead halide perovskite solar cells (PSCs) have recently attracted tremendous interest in the renewable energy field, owing to their easy-fabrication, cost-effective opportunities, and outstanding optoelectronic properties.[1–4] Reaching a certified power conversion efficiency (PCE) of 25.5%[5] within the last decade, PSCs show performance on the lab scale, which is comparable to established photovoltaic (PV) technologies.

Highly-efficient PSCs mostly utilize the regular (n–i–p) architecture in mesoscopic configuration.[6–9] However, these devices still suffer from some issues such as poor long-term stability and current–voltage hysteresis, which indeed hinder the commercialization of the regular architecture.[10] To address these issues, choosing the inverted (p–i–n) architecture due to the cost-effectiveness and greatly suppressed

F. Sadegh, Prof. A. Hagfeldt, Dr. W. Tress
Laboratory of Photomolecular Science
Institute of Chemical Sciences and Engineering
École Polytechnique Fédérale de Lausanne
Lausanne CH-1015, Switzerland
E-mail: trew@zhaw.ch

F. Sadegh, Prof. M. Moghadam, Dr. R. Keshavarzi, Prof. V. Mirkhani, Dr. M. Amini, Prof. S. Tangestaninejad, Prof. I. Mohammadpoor-Baltork
Department of Chemistry
University of Isfahan
Isfahan 81746-73441, Iran
E-mail: moghadamm@sci.ui.ac.ir; r.keshavarzi@chem.ui.ac.ir

The ORCID identification number(s) for the author(s) of this article can be found under https://doi.org/10.1002/adfm.202102237.

DOI: 10.1002/adfm.202102237

Dr. S. Akin
Department of Metallurgical and Materials Engineering
Karamanoglu Mehmetbey University
Karaman 70200, Turkey
E-mail: seckinakin@kmu.edu.tr

Dr. M. A. Ruiz-Preciado, Dr. H. Zhang, Prof. M. Graetzel
Laboratory for Photonics and Interfaces
Institute of Chemical Sciences and Engineering
École Polytechnique Fédérale de Lausanne
Lausanne CH-1015, Switzerland

Dr. E. Akman
Scientific and Technological Research & Application Center
Karamanoglu Mehmetbey University
Karaman 70200, Turkey

Dr. W. Tress
Institute of Computational Physics
Zurich University of Applied Sciences
Wildbachstr. 21, Winterthur 8401, Switzerland

hysteresis effect has been becoming more and more attractive in the perovskite community.[11,12] In addition, some other aspects about inverted PSCs such as removing ionically doped hole transport materials and high operational stability have attracted wide research interests in the field and hint at a promising future.[13–15] Despite these attractions, such inverted PSCs currently possess inferior PCE compared to their conventional counterpart. Among the different approaches, inspired by the regular architecture, the employment of a mesoscopic configuration in inverted devices could play a key role to open up new opportunities to further improve performance and reduce the efficiency gap between regular and inverted structures.

Compared to inverted planar PSCs, in the mesoscopic counterpart, the mesoporous hole transport layer (HTL) works as a scaffold for the perovskite absorber as well as a transport channel for photo-excited holes. The mesoscopic HTL facilitates perovskite infiltration, enhances light-harvesting efficiency, and improves the interface between the HTL and perovskite layer.[16] The better contact between HTL and perovskite promotes the growth of the perovskite film leading to better surface coverage with high-quality grains, which effectively increases charge extraction, accelerates charge transportation, and suppresses trap-assisted recombination at the corresponding interface. The confluence of such improvements results in a significant PV performance, negligible hysteresis, good reproducibility, and prolonged stability.[17,18]

Since efficient charge extraction by a high-quality and stable HTL with appropriate interface properties is essential in PSCs, enhanced device performance could be achieved by designing promising semiconductor nanostructures as HTLs. Metal oxide-based *p*-type semiconductors are suitable alternative materials for HTLs in PSCs owing to their wide bandgap, high carrier mobility, good chemical stability, suitable energy levels, low-cost, and environmental friendliness.[19] Among the various candidates, inorganic NiO_x demonstrated a promising potential due to its large bandgap ranging from 3.6 to 4.0 eV, acceptable hole mobility (10^{-5} to 10^{-3} cm^2 V^{-1} s^{-1}), favorable energy level alignment, and high work function as high as 5.4 eV.[20,21] These properties prevent the perovskite layer from UV exposure and reduce the charge accumulation at the HTL/perovskite interface, resulting in efficient and stable devices.[22] Various methods have been devoted to further improve the efficiency in inverted PSCs based on planar nickel oxide HTLs such as surface modification, employment of interlayer, or doping with suitable dopants.[23,24] Nevertheless, only very few reports reached the high-efficiency of PSCs in the regular configuration. Therefore, the development of new strategies allowing for the fabrication of highly efficient and stable inverted NiO_x-based PSCs is still in great demand. As mentioned above, there lies a vast scope of improvement in inverted PSCs by introducing the mesoporous scaffold to the structure.

Hitherto, inverted PSCs with mesoporous-NiO_x (mp-NiO_x) HTL have rarely been reported (Table S1, Supporting Information) in contrast with their planar counterparts. Therefore, rigorous research effort is needed to further investigate the benefits of the mesoscopic architecture on the efficiency in parallel with the stability of inverted devices to meet the requirements for commercialization of this technology. In the first pioneering work, Wang et al. introduced inverted PSCs based on the bilayer structure containing sol-gel derived electron blocking-NiO_x (bl-NiO_x) layer and mp-NiO_x layer prepared by spin coating of diluting slurry commercial NiO_x nanopowder, ethyl cellulose, and terpineol which achieved a PCE of 9.5%.[25] In a follow-up study, they replaced the sol-gel derived bl-NiO_x with a sputtered bl-NiO_x film and increased the PCE to 11.6%.[26] In a similar direction, Guo et al. used solution derived $Ni(OH)_2$ nanosheets obtained from a mixture of $NiCl_2 \cdot 6H_2O$ and NaOH to PH 10 as the nickel source followed by using ethyl cellulose ethoce and alpha-terpineol where different annealing processes were applied to prepare the mp-NiO_x films with various morphologies. Finally, the champion device possessed a PCE of 11.97% based on a simple annealing process at 500 °C for 3h.[27] In another study, Yao et al. developed centimeter-sized PSCs based on a bilayer structure of Cu-doped bl-NiO_x and Cu-doped NiO_x nanoparticle-based mesoporous layer synthesized by a chemical precipitation method utilizing $Ni(NO_3)_2.6H_2O$, $Cu(NO_3)_2.3H_2O$, and NaOH followed by calcination of the obtained powder at 270 °C to reach effective charge collection at the NiO_x/perovskite interface with minimized recombination loss.[28] This approach revealed the fabrication of high-efficiency PSCs (18.1%) with negligible hysteresis, accompanied by remarkable stability. Recently, an inverted PSC based on chemical bath deposited mp-NiO_x as HTL was fabricated. The substrate was vertically immersed into a beaker with an aqueous ammoniacal precursor solution containing $NiSO_4$ and $K_2S_2O_8$ to pH = 11 at room temperature followed by annealing the obtained film at 500 °C.[29] As a result, a PCE up to 16.7% was achieved with a high fill factor (FF) of 0.85 compared to devices based on a sprayed NiO_x film with PCE of 14.5%. The main reasons for the enhanced performances are ascribed to an improved interfacial adhesion between the perovskite and NiO_x layer, together with reduced charge recombination. Very recently, Yin et al. reported hydrothermally processed 3D mesoporous NiO_x nanowall-based PSCs contributing to better charge transport with lower interfacial energy loss. The hydrothermal process was carried out at 65 °C of vertically immersed FTO glass into the aqueous solution of $NiCl_2$, $CO(NH_2)_2$, and $K_2S_2O_8$ in autoclave followed by annealing the products at 350 °C in air to transform into NiO_x nanowall-based films. This strategy significantly improved the interface contact with low defect density and enhanced the quality of the perovskite layer. As a result, a considerable efficiency of ≈18% was achieved, which further increased to 19.16% in the presence of a diethanolamine interface passivation layer.[30] Although these studies exhibit the critical impact of the morphology of the selective contact on the charge transfer and interfacial properties in PSCs, the requirement of vacuum-processing and complicated multi-step procedures remain challenges that hinder their commercialization.

Compared to traditional synthetic methods, the template-assisted strategy has become one of the straightforward and low-cost routes of synthesizing mesoporous materials. Through this method, templates are used as structure-directing agents and removed from the structure to create pores in the framework after the annealing procedure.[31] In this regard, non-ionic amphiphilic block copolymer (BC) templates can be proposed as an efficient strategy in the synthesis of well-defined mesoporous frameworks owing to their advantages such as facile removal features and diversity of molecular structures leading to a wide range of pore architectures.[32,33] Benefiting from the BC template-assisted synthesis concept, the mesoporous structures containing large mesopores in a broad range of diameter could be designed for different applications, which require the storage or hosting

of large-sized species/molecules.[34] Most promisingly, the BC template protocols allow the fabrication of homogenous, crack-free, and robust mesoporous films with uniformly distributed nanoparticles and normal pore size distribution through a facile single-step sol-gel method.[35] Furthermore, by adding the BCs to the sol-gel solution, the novel templated mesoporous structures are expected to offer a highly positive impact on the transparency of the photoelectrode.[35] It is worth noting that according to the best of our knowledge, there has been no report on utilizing mp-NiO_x films prepared via the template-assisted method exploiting triblock copolymers in inverted PSCs so far.

In this study, we successfully fabricated highly efficient and stable inverted PSCs in the mesoporous architecture by applying a sol-gel derived mp-NiO_x HTL utilizing pluronic triblock copolymer P123 as a template. The fabricated PSCs with regards to a bilayer structure of sol-gel derived compact NiO_x (c-NiO_x) electron blocking layer and templated mp-NiO_x HTL translated into an outstanding efficiency of 20.2%. Notably, the high performance obtained for our mesoscopic devices was achieved without interface passivation or doping strategies; and it is among the highest efficiencies for mp-NiO_x-based inverted PSCs reported to this date. Moreover, it is also important to highlight that the absorber and the charge transport layers were prepared through solution processing, paving the way for a highly efficient, low-cost, and scalable PV technology. Furthermore, adopting this breakthrough approach enabled a substantially suppressed hysteresis effect in inverted planar NiO_x-based PSCs. In addition, the mesoscopic devices with mp-NiO_x retained more than 90% of their initial efficiencies after a stability test by being subjected to a 35 ± 5% relative humidity at 25 °C over the span of 950 h under dark conditions without any encapsulation whereas the PCE of planar control devices dropped to 83% under the same aging conditions. Overall, considering all of the above-mentioned factors, we strongly believe that this study demonstrates the potential of templated mp-NiO_x films as highly efficient, stable, and easily fabricated HTLs for inverted PSCs.

2. Results and Discussion

Herein, a facile sol-gel derived mp-NiO_x film utilizing pluronic triblock copolymer P123 was developed and employed as the mesoscopic HTL in inverted PSCs with a bilayer structure of c-NiO_x/mp-NiO_x (Experimental details are presented in Supporting Information). Pluronic triblock copolymer P123 consists of hydrophilic poly(ethylene oxide) (PEO) and hydrophobic poly(propylene oxide) (PPO) blocks which are arranged in a $(PEO)_{20}(PPO)_{70}(PEO)_{20}$ triblock structure. Amphiphilic surfactant molecules dispersed in the hydrophilic medium form an aggregate with the hydrophilic regions in contact with the surrounding medium, sequestering the hydrophobic region in the micelle center. The inorganic phase containing terminal hydroxyl groups acts as hydrophilic nano building blocks which interact with the hydrophilic portion of the block copolymer through hydrogen bonding. Spin coating of the solution on the substrate leads to the formation of an organic–inorganic hybrid phase which is followed by the calcination process resulting in complete removal of the organic template from the film.

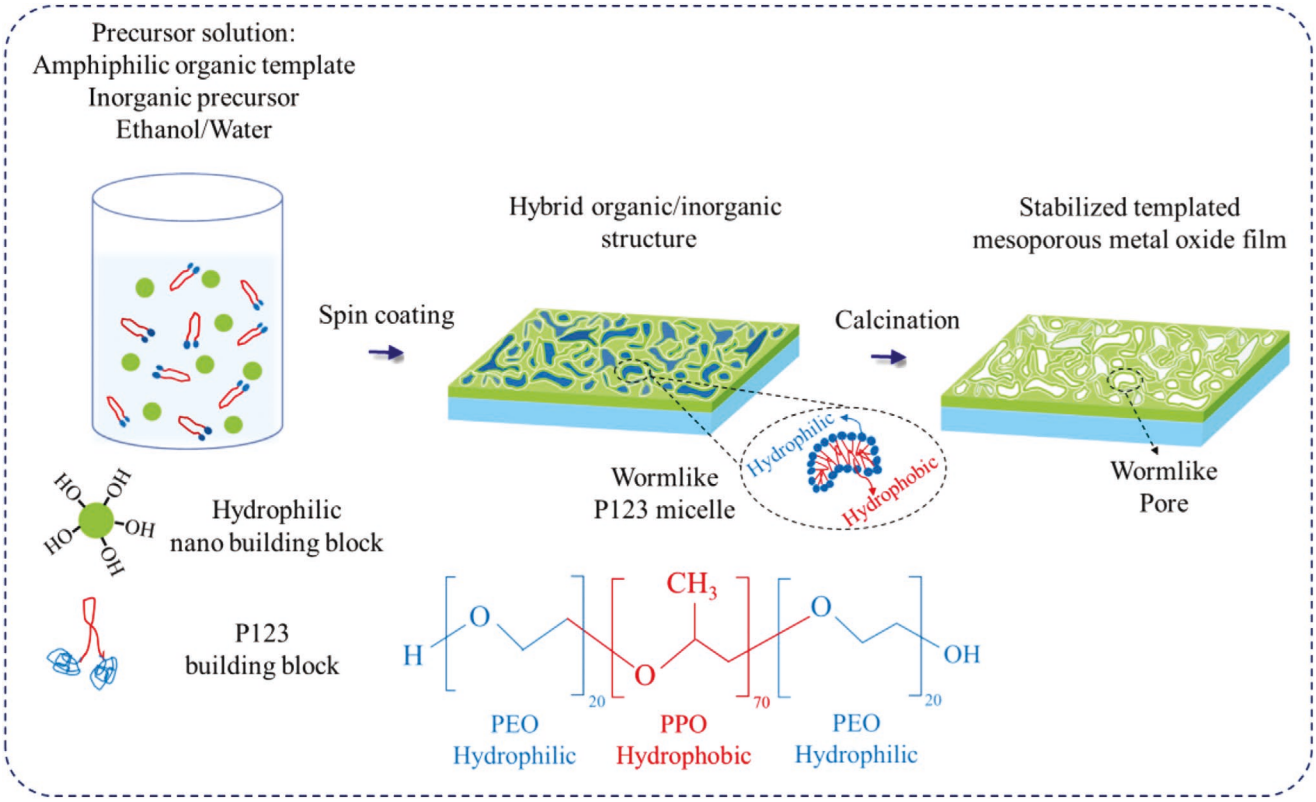

Figure 1. An illustration of the elaboration process to prepare P123 templated disordered mesoporous metal oxide film.

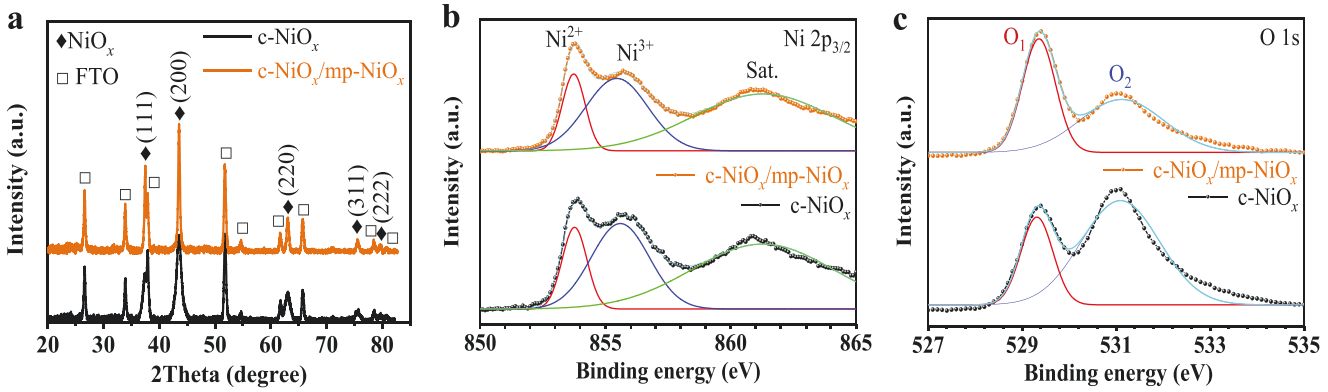

Figure 2. a) XRD patterns of the c-NiO$_x$ and c-NiO$_x$/mp-NiO$_x$ films deposited on FTO substrate. High-resolution XPS spectra of b) Ni 2p and c) O 1s peaks of the corresponding samples.

The mesoporous structure is thus obtained at once. **Figure 1** illustrates the process to prepare P123 templated disordered mesoporous metal oxide films. Structural and electrical characterization of the corresponding layers were performed before discussing the PV part to clearly understand the impact of the mesoporous layer on the interfacial and surface properties.

To confirm whether residual surfactant fragments are present after the calcination treatment, Fourier Transform Infra Red (FT-IR) spectroscopy was carried out. Figure S1, Supporting Information, reveals the presence of P123 surfactant associated with bands around 2870–2970 cm^{-1} and 1100 cm^{-1} in the as-synthesized mesoporous sample. These bands are related to stretching vibrations of C—H and C—O—C bonds, respectively, which are the most significant signals associated with P123 copolymer.[36] However, these P123-associated bands are no longer detectable after calcination of the mesoporous sample, which proves complete removal of the template structure after thermal treatment. The absorption band associated with the Ni—O vibration bond should appear close to 400 cm^{-1} but due to spectral limitations, this band cannot be observed.[37] It is noteworthy that the spectrum of the calcined mesoporous sample is similar to the spectrum of the compact sample used as control, reinforcing the evidence of complete template removal after calcination.

Crystallographic information of the samples was acquired by X-ray diffraction (XRD) analysis. **Figure 2**a shows the obtained patterns of c-NiO$_x$ and bilayer c-NiO$_x$/mp-NiO$_x$ films deposited on an FTO substrate. There are five narrow and strong peaks assigned to the (111), (200), (220), (311), and (222) plane orientations of crystalline NiO$_x$ with cubic structure (JCPDS card no: 047-1049). Utilizing the Debye–Scherrer equation, the typical crystallite sizes were estimated to be around 20 and 28 nm corresponding to compact and bilayer NiO$_x$ samples, respectively.

To elucidate the chemical composition of sol-gel-derived NiO$_x$ films, the compact and bilayer NiO$_x$ samples were studied by X-ray photoelectron spectroscopy (XPS), (Figures 2b,c). Figure 2b displays almost the same high-resolution XPS spectra of the Ni 2p$_{3/2}$ core level for both samples which consist of the main component with the double-peak feature at lower binding energy where deconvoluted to two peaks at ≈853.7 and ≈855.5 eV ascribed to Ni^{2+} and Ni^{3+} cations respectively, while a broad peak at higher binding energy ≈863.3 eV is ascribed to a shakeup process in the NiO$_x$ structure.[38] The Ni^{2+} cation is attributed to the standard Ni—O octahedral bonding in the rock-salt cubic configuration whereas the Ni^{3+} cation is assigned as a combination of the Ni^{2+} induced-vacancy, nickel hydroxides, and oxyhydroxides. It is worth noting that our results are consistent with those reported for other solution-processed NiO$_x$ films.[39] The high-resolution XPS spectrum of the O 1s core level splitting shown in Figure 2c consists of two deconvoluted peaks centered at ≈529.3 eV denoted as O$_1$ for Ni—O bonding in the NiO$_x$ lattice and ≈531.1 eV denoted as O$_2$ which is overlapping contributions of defect sites within the NiO$_x$ crystal lattice, nickel oxyhydroxides, hydroxides including defective nickel oxide with hydroxyl groups adsorbed on the surface, and organic oxygen.[40] As a comparison of two samples, the area ratio of O$_2$/O$_1$ decreased from 2.9 to 1.2 for the bilayer sample suggesting that the template-assisted process induces greater NiO$_x$ crystallinity and fewer defects at surface and grain boundaries. Such improvements especially fewer traps originated from undercoordinated oxygen atoms close to Ni vacancies in the lattice, which is a key issue for the sol-gel-driven metal oxides, are beneficial for efficient hole extraction from perovskite to HTL.[41]

Transmission electron microscopy (TEM) was applied to further investigate the templated mp-NiO$_x$ materials (**Figure 3**a). It could be seen that NiO$_x$ particles have an average diameter of ≈26 nm (Figure S2a, Supporting Information). Similarly, the corresponding high-resolution TEM image in Figure 3b identifies an excellent crystallinity with a lattice fringe with interplanar distances of ≈2.4 and ≈2.06 Å, in accordance with the (111) and (200) crystal planes of the NiO$_x$ structure, respectively. As shown in Figure 3c, the corresponding selected area electron diffraction (SAED) pattern under TEM further confirms the crystalline nature of the mp-NiO$_x$ film where the well-determined diffraction rings imply the polycrystalline nature of the mp-NiO$_x$ crystals as shown in XRD patterns. We could infer that a well crystalline mp-NiO$_x$ with definite pore size and shape can be synthesized by the copolymer template-assisted sol-gel method in our experiment.

We investigated the morphological surface features of the compact and bilayer NiO$_x$ films deposited on FTO substrate using scanning electron microscopy (SEM) and presented micrographs in Figures 3d,e. The top-view SEM micrograph of the compact sample (Figure 3d) exhibits a typical surface morphology compared to similar studies[29,42] showing the

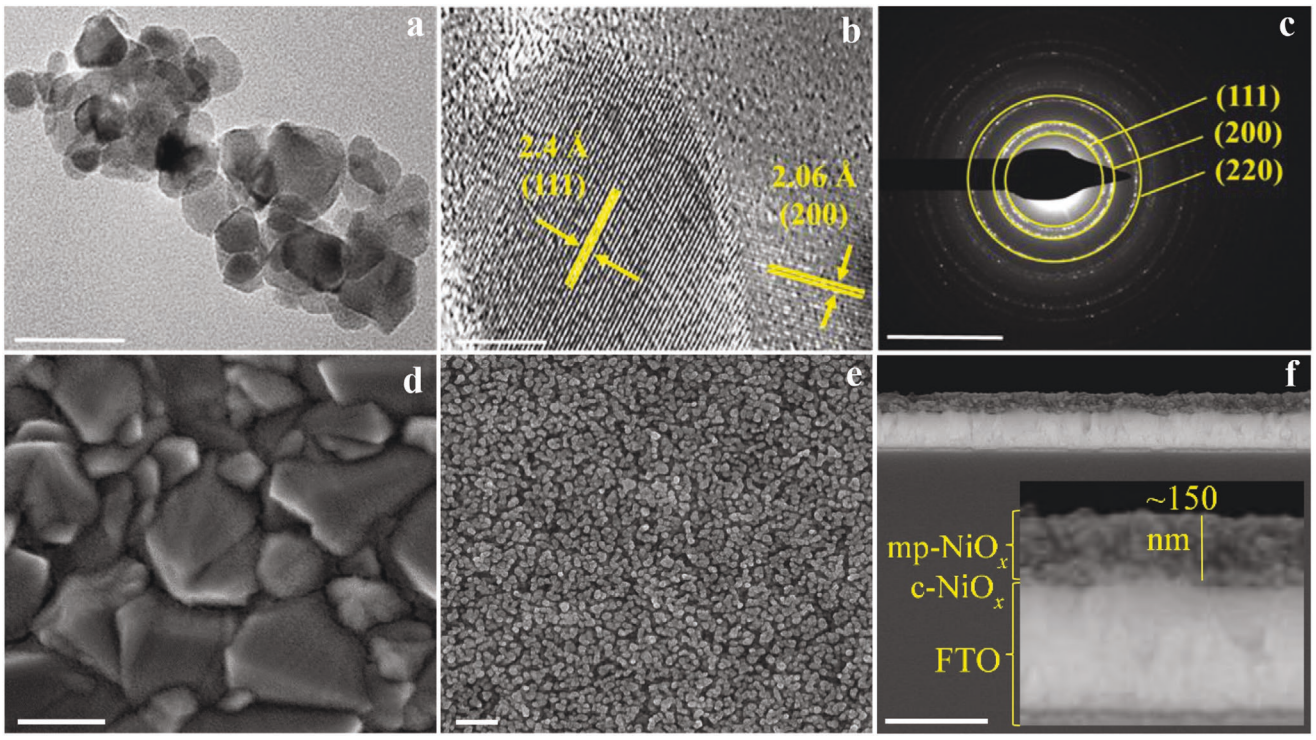

Figure 3. a) TEM image (scale bar is 50 nm), b) HR-TEM image (scale bar is 5 nm), and c) SAED pattern (scale bar is 10 nm^{-1}) of mp-NiO$_x$ sample. Top-view SEM images of d) c-NiO$_x$ and e) c-NiO$_x$/mp-NiO$_x$ films deposited on FTO substrate (scale bars in both SEM images are 200 nm). f) Cross-sectional SEM image of c-NiO$_x$/mp-NiO$_x$ film deposited on FTO substrate (scale bar is 1 µm); inset shows the magnified view.

outlines of FTO grains. The micrograph of the bilayer NiO$_x$ sample presented in Figure 3e reveals that the templated mesoporous layer has clearly a high degree of porosity composed of a disordered worm-like interconnected mesoporous network which is uniformly distributed in the nanosized NiO$_x$ particles. The particle and pore diameter distribution histograms (Figure S2b, Supporting Information) of the mp-NiO$_x$ film obtained from the SEM image show an average particle and pore diameter of ≈30 ± 7 and ≈31 ± 11 nm, respectively. The narrow-size distributions point out good uniformity in particles and pore diameters through this template-assisted method which is beneficial for preparing a uniform mesoporous framework. Moreover, most of the particles visible in the SEM image are 25–30 nm in diameter, which is consistent with the size obtained from the XRD pattern indicating that most of the particles are not composed of different crystalline domains but are individual crystals. Furthermore, the elemental mapping image (Figure S3, Supporting Information) exhibits a homogeneous distribution of Ni and O elements within the templated mp-NiO$_x$ film. Specifically, the cross-sectional SEM micrograph of mp-NiO$_x$ film deposited on FTO/c-NiO$_x$ substrate (Figure 3f) suggests a largely continuous, uniform, and crack-free 150 nm thick layer without gap at the substrate/mp-NiO$_x$ interface indicating homogeneous coating and a high-quality mp-NiO$_x$ film prepared by P123 template, which is promising for high-quality perovskite formation. In contrast to the compact thin film, the mp-NiO$_x$ film thanks to the mesoporous channels exhibit a higher surface area for perovskite filling and crystallization.

For PV applications, it is crucial that the charge transport layers possess adequate optical properties. In particular, when working with inverted PSCs, the transmittance of the HTL must be maximized and the reflectance minimized. In this regard, the optical transparency and reflectivity of the c-NiO$_x$ and bilayer c-NiO$_x$/mp-NiO$_x$ films deposited on an FTO substrate were characterized by UV–Vis spectroscopy, as shown in **Figure 4**a. The spectra demonstrate a negligible effect on the optical properties of the FTO/c-NiO$_x$ compared to the bare FTO substrate. On the other hand, the transmittance of the c-NiO$_x$/mp-NiO$_x$ bilayer structure is higher than that of the bare FTO and compact HTL. This can be explained by the fact reported in previous studies that the refractive index of a material decreases when introducing mesoscale pores into the framework.[43] In other words, the resulting enhanced transparency can be explained by an index matching effect of the mesoporous structure.[35,44] The diffuse reflectance spectra shown in Figure 4a confirm a reduction of the reflectance over the entire wavelength range in the presence of mesoporous templated mp-NiO$_x$ layer. Besides, the optical band gap (E_g) values of c-NiO$_x$ and bilayer c-NiO$_x$/mp-NiO$_x$ films deposited on FTO substrate were estimated to be 3.92 eV by Tauc analysis (Figure 4b) as consistent with values reported in the literature.[45]

To investigate the effect of the different NiO$_x$ films on the quality and surface morphology of the perovskite film, SEM micrographs, XRD patterns, and UV–Vis spectra of perovskite layers deposited on FTO/c-NiO$_x$ and FTO/c-NiO$_x$/mp-NiO$_x$ substrates were also examined. As seen, the top view SEM micrograph of the perovskite film on c-NiO$_x$/mp-NiO$_x$ substrate

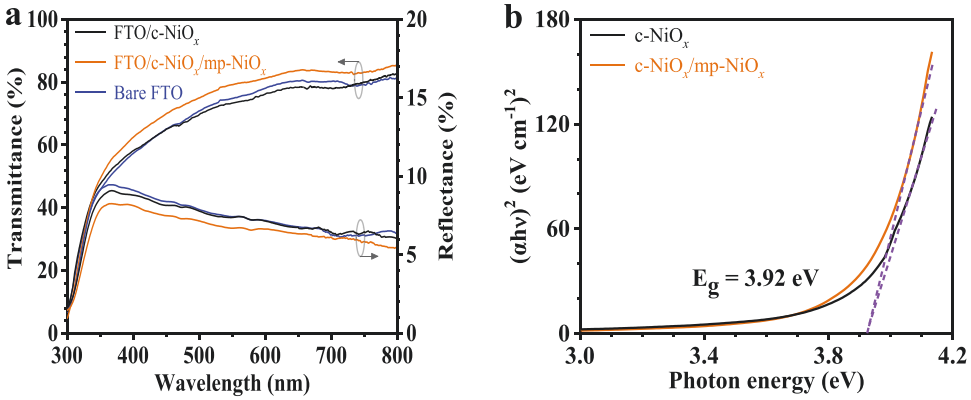

Figure 4. a) UV–Vis transmittance and reflectance spectra of bare FTO, FTO/c-NiO_x, and FTO/c-NiO_x/mp-NiO_x samples. b) The extrapolated plot of $(\alpha h\upsilon)^2$ against hυ obtained from the absorbance of c-NiO_x and bilayer c-NiO_x/mp-NiO_x films deposited on FTO substrate.

(**Figure 5**b) clearly exhibits a full surface coverage with compact and pinhole-free morphology whereas some pinholes can be clearly seen in the SEM micrograph of c-NiO_x/perovskite film (Figure 5a). As is known, pinholes on perovskite are shown to increase the shunting problem and decrease V_{oc}.[46] Moreover, grain size and crystal structure of the perovskite film are other important parameters for achieving high-performing devices, which are substantially affected by perovskite film formation.[47] The corresponding size distributions of perovskite grains, depicted in Figure 5c, display an average perovskite grain size of ≈213 ± 83 and ≈263 ± 83 nm for compact and bilayer NiO_x films, respectively. The enlarged grains with a lower density of grain boundaries in the perovskite film on bilayer NiO_x substrate can be ascribed to the nucleation behavior promoting sustainable growth of more widely dispersed nuclei on the surface of the mesoporous film.[28] In other words, less restriction during crystal growth could be another reason for the increase in grain size for bilayer HTL, since the perovskite crystal domain size can be constrained by the pore size of preformed NiO_x scaffolds.[48] The XRD pattern was utilized to probe the crystallinity of the perovskite films and the typical peaks presented in Figure S4a, Supporting Information, confirm the successful formation of the perovskite phase. Specifically, the higher peak intensity at 14.2° for perovskite film on the bilayer NiO_x substrate indicates a better crystallinity, which agrees with increased grain size deduced from the SEM results. The achieved high-quality perovskite layer with high crystallinity and large grains with fewer grain boundaries for bilayer NiO_x sample confirms a better film-formation ability of the ideal interconnected porous structure, which is superior to that of the

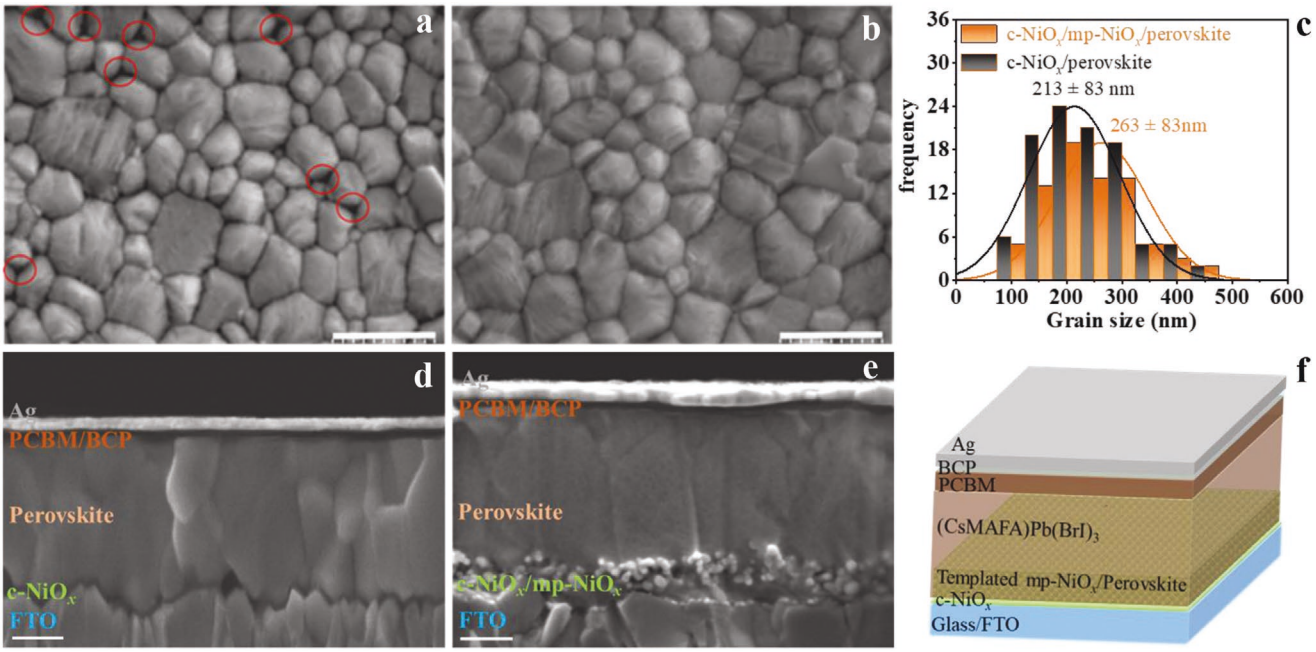

Figure 5. Top-view SEM images of the perovskite films deposited on a) c-NiO_x and b) c-NiO_x/mp-NiO_x HTLs (scale bar in both images is 500 nm). c) The corresponding histograms derived based on perovskite grain size obtained from the top SEM images. Cross-sectional SEM images of the d) planar and e) mesoscopic full devices (scale bar in both images is 200 nm). f) Schematic illustration of the meso-structured PSCs employed in this study.

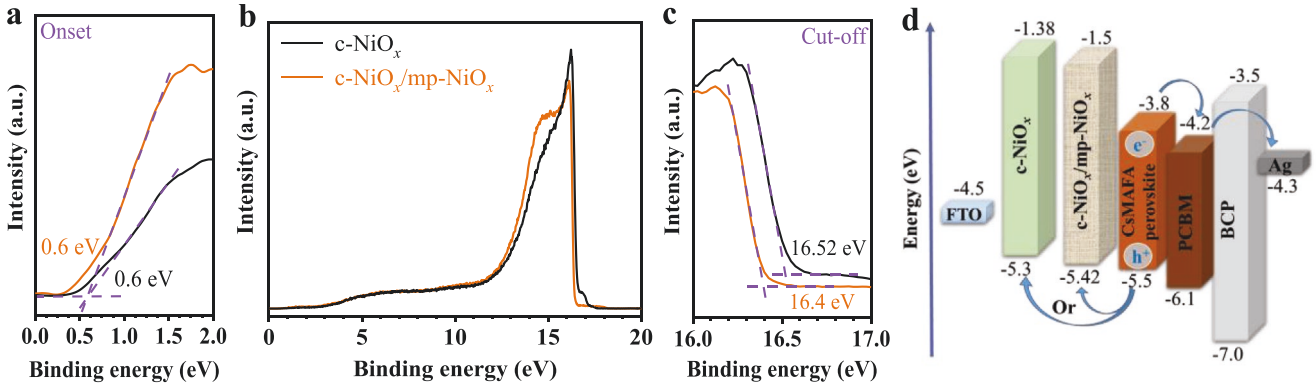

Figure 6. a) E_{onset}; the onset of photoemission in the low binding energy region b) UPS spectra, and c) $E_{cut\text{-}off}$; the inelastic cut-off binding energy of c-NiO_x and bilayer c-NiO_x/mp-NiO_x films deposited on FTO substrate. d) Energy level diagram of the typical device architecture.

c-NiO_x. Notably, the porous scaffold is beneficial to form a good physical contact with the perovskite film and improved HTL/perovskite interface, which plays a considerable role in hole transportation through the junction.[49] Additionally, the good surface morphology of such perovskite films with fewer grain boundaries effectively reduces interface defects which suppresses non-radiative charge recombination and facilitates the transport/collection of photogenerated charges in the device.[50]

Figure S4b, Supporting Information, presents the absorption spectra of perovskite films and the perovskite film deposited on c-NiO_x/mp-NiO_x HTL shows a higher absorbance across the entire region than that of the perovskite film on c-NiO_x HTL. This could be ascribed to the slightly thicker perovskite layer including the infiltrated part in the mesoscopic NiO_x, as can be seen in cross-sectional SEM photographs (Figures 5d,e).[25] To show a high degree of pore filling and better wettability of the mp-NiO_x film, the contact angle of a water droplet on both NiO_x samples was measured. As depicted in Figures S5a,b, Supporting Information, the contact angle on the bilayer NiO_x sample (33°) is considerably lower than that of the c-NiO_x sample (61°).

To further evaluate the morphology characteristics of the solar cells, we reported the cross-sectional SEM views (Figure 5d,e) of control and mesoscopic full devices, respectively. Here, the mesoscopic devices were fabricated in the typical structure of FTO/c-NiO_x/mp-NiO_x/$Cs_{0.05}(MA_{0.15}FA_{0.85})_{0.95}Pb(Br_{0.15}I_{0.85})_3$/PCBM/BCP/Ag (Figure 5f). In both SEM micrographs, the c-NiO_x layer is not visible due to the low thickness whereas in the mesoscopic device a rather conformal mp-NiO_x layer with full coverage within the entire range of the substrate is observable, which looks well infiltrated by the perovskite material. Besides, the mp-NiO_x/perovskite layer was covered by a highly uniform and continuous capping-layer advantageous for acquiring higher V_{OC}. Interestingly, this capping-layer of perovskite grains is highly compact where individual grains extend from top to bottom consistent to the enlarged grains with fewer grain boundaries shown in the top view image. Unlike the mesoscopic device, the planar structure consists of a multi-grain perovskite film with a smaller grain size and more grain boundaries. Additionally, a gap between the perovskite layer and the substrate is visible (Figure S6a,b, Supporting Information) which can be detrimental to device performance. As mentioned above, the high-quality perovskite film in mesoscopic device is expected to lead to better charge transport as well as fewer recombination losses along grain boundaries.[51]

Ultraviolet photoelectron spectroscopy (UPS) spectra were recorded to probe the hole extraction ability of c-NiO_x and bilayer c-NiO_x/mp-NiO_x HTLs as shown in **Figure 6**a–c. The Fermi levels (E_F) of compact and bilayer samples are estimated as –4.70 and –4.82 eV, respectively, according to the equation of $E_F = E_{cut\text{-}off}$ (cut-off binding energy) – 21.22 eV (emission energy from He irradiation). The valence band maximum (E_{VB}) of NiO_x films is measured to be –5.3 eV for compact and –5.42 eV for bilayer samples, following the equation of $E_{VB} = E_F - E_{F,\,edge}$. The conduction band minimum (E_{CB}) of the films, calculated from the bandgap (E_g), shown in Figure 4b, is obtained as –1.38 and –1.5 eV for compact and bilayer samples, respectively. The energy levels of all involved materials are presented in Figure 6d. It is found that in contrast to c-NiO_x film, there is a downward shift of the valance band in the case of bilayer NiO_x HTL which is believed to be more compatible with the valance band of the CsMAFA perovskite film (–5.5 eV) and might lead to reduced interface recombination.

For the thickness optimization, the concentration of the NiO_x precursors was varied and the optimum concentration selected based on the efficiency. PV parameters are presented in Figure S7, Supporting Information. Thereafter, mesostructured PSCs have been fabricated with this optimized concentration for further analysis. We fabricated a series of inverted PSCs in planar and mesoscopic configuration to assess whether there is an effect of P123 templated mp-NiO_x scaffold on the device performance. A markedly improved PV performance was obtained in the mesoscopic devices over that of planar control devices. **Figure 7**a shows the current density–voltage (J–V) curves of the champion planar and mesoscopic PSCs based on NiO_x HTLs running a scan with rates of 50 mV s^{-1} under full sun illumination (100 mW cm^{-2}) from which we deduced the corresponding PV parameters listed in **Table 1**. The champion planar device exhibits a short-circuit photocurrent density (J_{SC}) of 22.9 mA cm^{-2}, an open-circuit voltage (V_{OC}) of 1.05 V, and a FF of 77%, yielding a PCE of 18.7% (under reverse scan). Remarkably, the champion mesoscopic device based on templated mp-NiO_x shows higher PV parameters: a J_{SC} of 23.8 mA cm^{-2}, a V_{OC} of 1.09 V, an FF of 79%, and a PCE of 20.2% (under reverse scan).

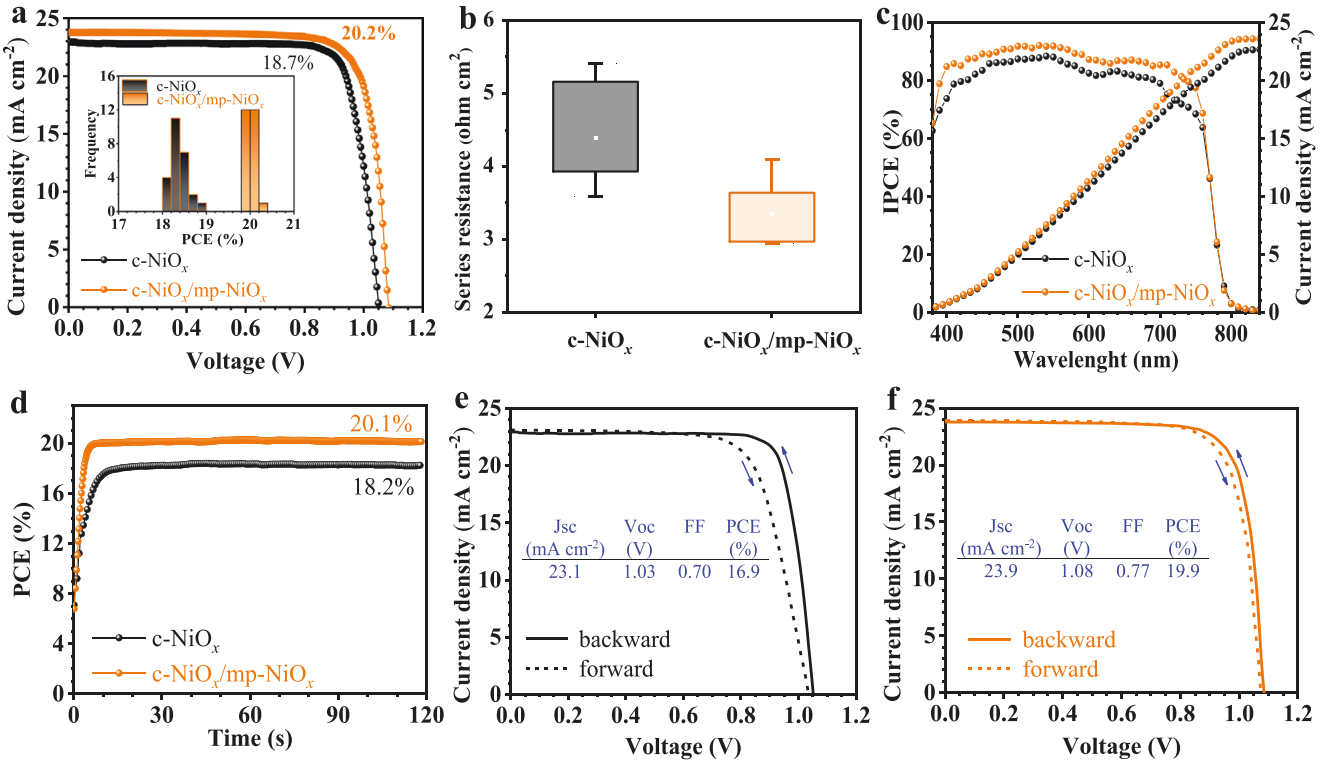

Figure 7. (a) *J–V* characteristics of the best-performing PSCs based on different HTLs measured in reverse direction with the scanning rate of 50 mV s^{-1}. The inset shows the statistics of PCE over 25 devices in each case. b) Series resistance extracted by the slope of the *J–V* curves at V_{OC}. c) IPCE curves of planar and meso-structured PSCs and the integrated J_{SC} values obtained from the respective IPCE spectra. d) The SPO curves of the planar and meso-structured PSCs. Hysteresis characteristics of the corresponding e) planar and f) meso-structured PSCs. The insets show PV parameters of performing devices obtained by forward scan direction.

To the best of our knowledge, this PCE value in our mesoscopic device without any interface passivation or dopant strategy is one of the highest efficiencies among the inverted mesoscopic PSCs based on NiO_x HTL (Table S1, Supporting Information).

Obviously, introducing the mp-NiO_x layer to the device enhances all PV parameters. The significant enhancement in the V_{OC} could be attributed to reduced trap-assisted charge recombination at defects at the grain boundaries of the perovskite and/or at the HTL/perovskite interface.[52] Similarly, higher FF can be attributed to the lower overall series resistance of the cell associated with close connection between the high-quality perovskite layer and mp-NiO_x film, which is beneficial to charge transport and collection.[53] To assess resistive losses, the differential resistance was extracted at V_{OC} for *J–V* curves measured under simulated sunlight. Figure 7b demonstrates that the mp-NiO_x scaffold leads to a reduction in the overall series resistance of the mesoscopic PSCs in contrast to the planar counterpart as consistent with the increased FF. The advances in the PV performance of the inverted NiO_x-based PSCs are also confirmed by the incident photon-to-current conversion efficiency (IPCE) and stabilized power output (SPO) analyses. Figure 7c presents the corresponding IPCE spectra of the champion devices. Both devices possess a broad IPCE plateau (>80%) over a wide spectral range. However, the spectrum of mp-NiO_x device shows a high IPCE of around 95% in some wavelengths. This value is higher than the transmission reported in Figure 4a, which is mainly due to the scattering effect of our hazy FTO substrate, reducing the direct transmission in a transmission measurement, but leading to light trapping and absorption in the adjacent perovskite film. However, a notable improvement in IPCE and the acquired outstanding J_{SC} can be seen in mp-NiO_x incorporated devices independent of wavelength, signifying not only the higher light absorption of the perovskite film but more importantly an enhanced charge extraction. The integrated J_{SC} from the IPCE measurements reaches 22.7 and 23.6 mA cm^{-2} for control

Table 1. PV parameters of the best-performing planar and meso-structured PSCs extracted from the reverse *J–V* scan and corresponding average values.

HTL	V_{OC} [V]		J_{SC} [mA cm^{-2}]		FF		PCE [%]	
	Champion	Average	Champion	Average	Champion	Average	Champion	Average
c-NiO_x	1.05	1.05 ± 0.01	22.9	22.8 ± 0.1	0.77	0.76 ± 0.01	18.7	18.4 ± 0.2
c-NiO_x/mp-NiO_x	1.09	1.08 ± 0.01	23.8	23.7 ± 0.1	0.79	0.78 ± 0.01	20.2	20.0 ± 0.1

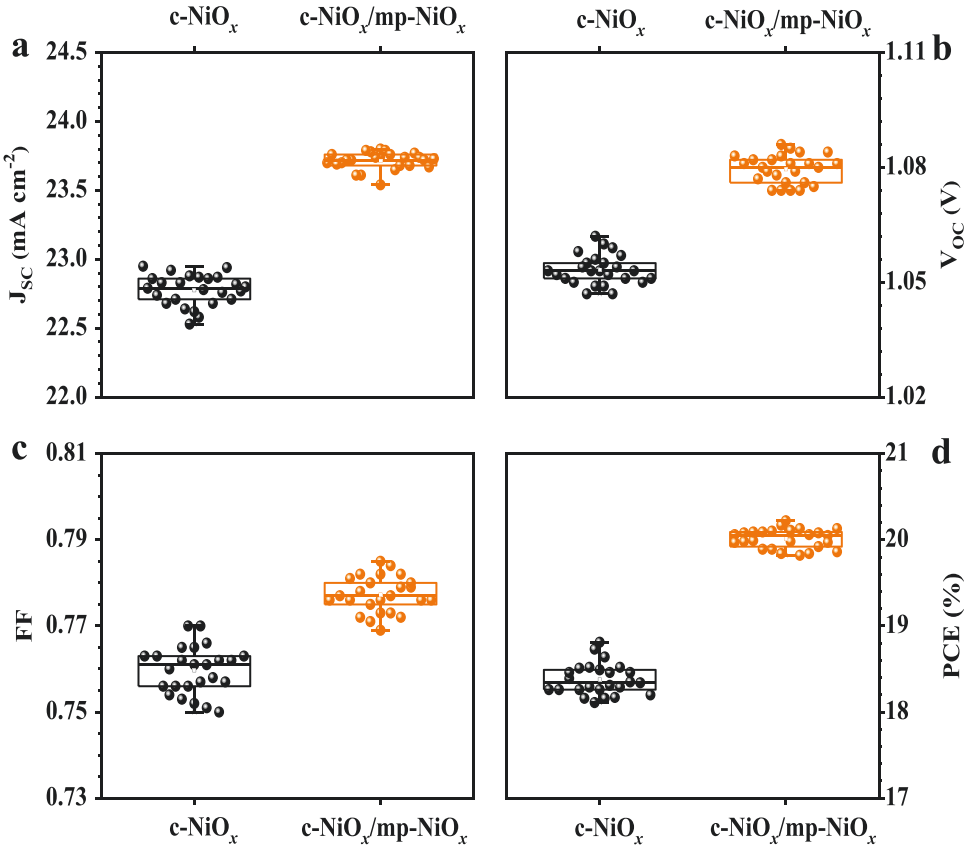

Figure 8. PV metrics of planar and meso-structured devices (25 devices for each case): a) J_{SC}, b) V_{OC}, c) FF, and d) PCE.

and mesoscopic cells, respectively, which is substantially consistent with *J–V* measurements (Figure 7a). The SPO was conducted for the best-performing devices at their maximum PCE under the standard illumination (AM 1.5G) over 120 s. As depicted in Figure 7d, the PCE of control PSC stabilizes at ≈18.2%, whereas the mesoscopic PSC yields a stabilized PCE of ≈20.1%.

As the PV parameters could be dependent on scan direction resulting in hysteresis phenomena, in Figure 7e,f, we showed forward and reverse *J–V* curves of the best-performing planar and mesoscopic devices to determine the hysteresis index (HI), where the extracted PV parameters under the forward scan are summarized in the inset. The HI was calculated using Equation (1):

$$\text{Hysteresis index} = (\text{PCE}_{\text{backward}} - \text{PCE}_{\text{forward}})/\text{PCE}_{\text{backward}} \quad (1)$$

Remarkably, while the HI for the champion control device was calculated to be 0.098, the champion mesoscopic device exhibited a negligible hysteresis effect with a calculated index of 0.018. The *J–V* hysteresis within PSCs can originate from structural defects in the perovskite absorber and the perovskite/charge transport layer interfaces. It is well known that interface defects act as traps for electrons and holes which could lead to a charge accumulation at the corresponding interface and also function as recombination centers, with rates influenced by ion migration.[54,55] As evidenced by SEM images (Figure 5a,b), the perovskite film deposited on bilayer c-NiO$_x$/mp-NiO$_x$ HTL possesses large grains and reduced grain boundaries, which can also alleviate hysteresis.[56]

To gain insights into the corresponding reproducibility of the PSCs of this study, the PV performance obtained with the planar and mesoscopic architectures was further ascertained by measuring 25 devices for each case, and statistics of PV parameters are summarized in **Figure 8** and Table 1. Moreover, the PCE histogram chart is given in the inset of Figure 7a. Specifically, average PCEs of 18.4 ± 0.2% and 20.0 ± 0.1% were attained for control and mesoscopic devices, respectively confirming high reliability (small standard deviation) in the presence of mp-NiO$_x$ HTL.

To elucidate the charge-transfer dynamics, time-resolved photoluminescence (TRPL) data were collected for the perovskite layers coated on bare FTO, FTO/c-NiO$_x$, and FTO/c-NiO$_x$/mp-NiO$_x$ substrates (**Figure 9**a). The PL decay of the NiO$_x$ samples was fitted by a bi-exponential model, whereas a single exponential model was sufficient for the perovskite on bare FTO. The obtained parameters are summarized in Table S2, Supporting Information. Evidently, the initial decay lifetime sharply decreased with the integration of HTLs from 90 ns for the bare FTO to 10 and 7 ns for c-NiO$_x$ and c-NiO$_x$/mp-NiO$_x$ HTLs, respectively. Compared to the compact counterpart (and bare FTO), the rapid quenching of bilayer HTL highlights the enhanced charge extraction by a faster charge transfer to the HTL. This can be ascribed to the improved contact between the mp-NiO$_x$ and perovskite due to a more conformal coverage (fewer voids) and a higher interface area due to the infiltration

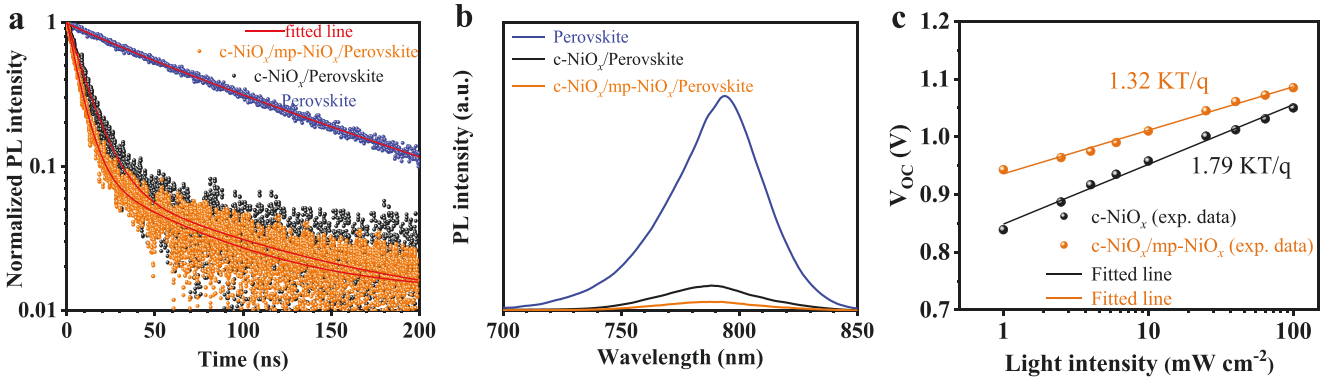

Figure 9. a) TRPL and b) PL spectra of perovskite films deposited on bare and NiO_x-coated FTO substrates. c) The light intensity dependence of the V_{OC} for planar and meso-structured PSCs.

of the perovskites into the mp-NiO_x film (see Figure 5). The steady-state PL spectra (Figure 9b) confirm this effect, where an enhanced contact with the mp-NiO_x leads to a stronger quenching of the PL, indicative of enhanced charge transfer with subsequent non-radiative recombination.[57] Comparing with an inverse trend of the V_{OC} (V_{OC} is higher for mp-NiO_x), we suspect that the larger PL in the c-NiO_x sample originates from luminescent regions that do not contribute to photocurrent.

For further analysis of the recombination mechanism, the V_{OC} was probed as a function of illumination intensity to deduce the ideality factor (n_{id}) (Figure 9c). In an ideal solar cell with only bimolecular charge recombination, the slope of the V_{OC} curve versus the natural logarithm of the incident light intensity (I) should be kT/q while a solar cell with trap-assisted charge recombination may show a slope greater than kT/q.[58] The n_{id} value is represented by Equation (2):

$$n_{id} = (q/kT)(dV_{OC}/d\ln I) \quad (2)$$

where q, k, and T are elementary charge, Boltzmann's constant, and temperature, respectively. As shown in Figure 9c, the mesoscopic PSC shows a significantly smaller ideality factor (1.32) as compared to that of the planar PSC (1.79). This indicates reduced trap-assisted recombination in the bulk of the perovskite and at the HTL/perovskite interface, which is consistent with the larger grains observed in SEM.[59,60]

In addition to the high PV efficiency, the durability of the PSCs for long-term applications is another major concern for commercialization aspects. In this regard, we compared the long-term stability of inverted PSCs based on bilayer NiO_x and control planar devices (4 devices for each case). The unencapsulated devices were stored in an ambient environment with a relative humidity of 35 ± 5% and a temperature of 25 °C. The performance of the devices was monitored after different storage times and the corresponding PV parameters are demonstrated in **Figure 10**. The results show that mesoscopic devices achieved a noticeable enhancement in stability compared to the planar PSCs. Specifically, the mesoscopic devices remained 90% of their initial efficiencies after 950 h of storage, while the control PSCs degraded to 83% under the same conditions. As can be seen, V_{OC} values do not decline too much whereas the maximum degradation of PCE stems from the reduction of FF and J_{SC} which can be related to reduced charge transport due to interfacial degradation. The improved perovskite quality with a film composed of larger grains and fewer structural defects could render the resulting PSC less susceptible to moisture uptake and reduce the vulnerability of the perovskite layer induced by atmospheric moisture in mesoscopic devices.[61,62] The suppression of ion migration owing to the high surface quality of perovskite layer can be another reason for the improvement in the stability of devices.

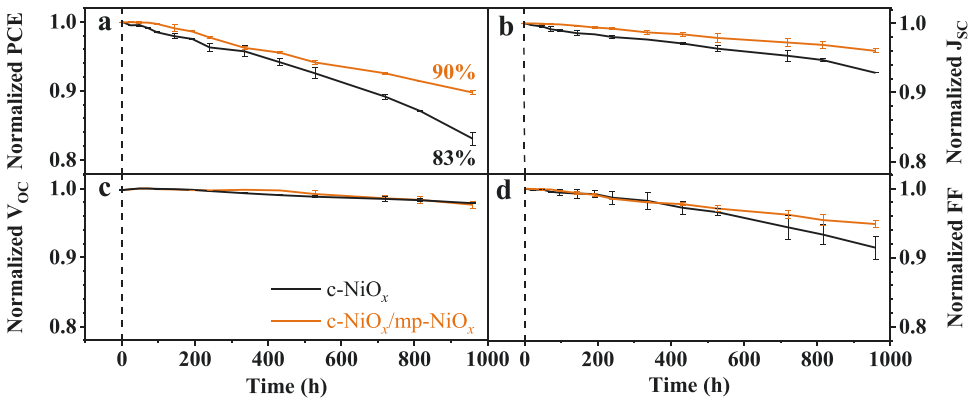

Figure 10. Normalized a) PCE, b) J_{SC}, c) V_{OC}, and d) FF curves of performing planar and meso-structured devices without any encapsulation stored at 35 ± 5% relative humidity and 25 °C over 950 h under dark (4 devices for each case).

3. Conclusions

In this study, an efficient and stable mesoporous NiO_x film was synthesized via a facile and low-cost triblock copolymer template-assisted strategy and successfully employed to inverted PSCs for the first time. Such high-quality mp-NiO_x scaffold significantly improved the perovskite crystal growth, facilitating charge transportation and suppressing charge recombination. As a result, champion mesoscopic inverted PSC achieved a high PCE of 20.2% with negligible hysteresis. In addition, the devices based on templated mp-NiO_x HTL retained more than 90% of their initial PCEs without any encapsulation at 35 ± 5% relative humidity over 950 h under dark conditions, whereas the PCEs of the planar devices dropped to 83%. This study highlights the potential of the copolymer template-assisted strategy for synthesizing mesoscopic metal oxides as promising HTLs for highly efficient and stable mesoscopic PSCs in inverted architecture.

Supporting Information

Supporting Information is available from the Wiley Online Library or from the author.

Acknowledgements

F.S. acknowledges the Ministry of Science, Research and Technology of Iran and Iranian Nano Technology Initiative Council for financial support. The authors gratefully thank Dr. Dan Ren from LPI, EPFL for his help in performing TEM analysis.

Conflict of Interest

The authors declare no conflict of interest.

Data Availability Statement

Research data are not shared.

Keywords

hole transport layers, inverted architecture, mesoscopic PSCs, template-assisted strategy, triblock copolymers

Received: March 5, 2021
Revised: April 30, 2021
Published online: June 10, 2021

[1] S. Akin, F. Sadegh, S. Turan, S. Sonmezoglu, *ACS Appl. Mater. Interfaces* **2019**, *11*, 45142.
[2] S. D. Stranks, G. E. Eperon, G. Grancini, C. Menelaou, M. J. P. Alcocer, T. Leijtens, L. M. Herz, A. Petrozza, H. J. Snaith, *Science* **2013**, *342*, 341.
[3] A. E. Shalan, E. Akman, F. Sadegh, S. Akin, *J. Phys. Chem. Lett.* **2021**, *12*, 997.
[4] E. Akman, S. Akin, *Adv. Mater.* **2021**, *33*, 2006087.
[5] NREL Solar Cell Efficiency Chart, **2021**, https://www.nrel.gov/pv/assets/pdfs/pv-efficiency-chart.20200925.pdf.
[6] Y. Liu, S. Akin, L. Pan, R. Uchida, N. Arora, J. V. Milić, A. Hinderhofer, F. Schreiber, A. R. Uhl, S. M. Zakeeruddin, A. Hagfeldt, M. I. Dar, M. Grätzel, *Sci. Adv.* **2019**, *5*, 2543.
[7] E. Akman, A. E. Shalan, F. Sadegh, S. Akin, *ChemSusChem* **2021**, *14*, 1176.
[8] S. Akin, E. Akman, S. Sonmezoglu, *Adv. Funct. Mater.* **2020**, *30*, 2002964.
[9] L. Xiong, M. Qin, C. Chen, J. Wen, G. Yang, Y. Guo, J. Ma, Q. Zhang, P. Qin, S. Li, G. Fang, *Adv. Funct. Mater.* **2018**, *28*, 1706276.
[10] W. Tress, N. Marinova, T. Moehl, S. M. Zakeeruddin, M. K. Nazeeruddin, M. Grätzel, *Energy Environ. Sci.* **2015**, *8*, 995.
[11] X. Zheng, Y. Hou, C. Bao, J. Yin, F. Yuan, Z. Huang, K. Song, J. Liu, J. Troughton, N. Gasparini, C. Zhou, Y. Lin, D.-J. Xue, B. Chen, A. K. Johnston, N. Wei, M. N. Hedhili, M. Wei, A. Y. Alsalloum, P. Maity, B. Turedi, C. Yang, D. Baran, T. D. Anthopoulos, Y. Han, Z.-H. Lu, O. F. Mohammed, F. Gao, E. H. Sargent, O. M. Bakr, *Nat. Energy* **2020**, *5*, 131.
[12] Y. Chen, W. Tang, Y. Wu, R. Yuan, J. Yang, W. Shan, S. Zhang, W.-H. Zhang, *Sol. RRL* **2020**, *4*, 2000344.
[13] J. A. Christians, P. Schulz, J. S. Tinkham, T. H. Schloemer, S. P. Harvey, B. J. Tremolet de Villers, A. Sellinger, J. J. Berry, J. M. Luther, *Nat. Energy* **2018**, *3*, 68.
[14] J. Ma, M. Zheng, C. Chen, Z. Zhu, X. Zheng, Z. Chen, Y. Guo, C. Liu, Y. Yan, G. Fang, *Adv. Funct. Mater.* **2018**, *28*, 1804128.
[15] Y. Chen, Z. Yang, S. Wang, X. Zheng, Y. Wu, N. Yuan, W.-H. Zhang, S. (Frank) Liu, *Adv. Mater.* **2018**, *30*, 1805660.
[16] M. Zhang, X. Cui, Y. Wang, B. Wang, M. Ye, W. Wang, C. Ma, Z. Lin, *Nano Energy* **2020**, *71*, 104620.
[17] F. Sadegh, S. Akin, M. Moghadam, V. Mirkhani, M. A. Ruiz-Preciado, Z. Wang, M. M. Tavakoli, M. Graetzel, A. Hagfeldt, W. Tress, *Nano Energy* **2020**, *75*, 105038.
[18] G. Yang, H. Lei, H. Tao, X. Zheng, J. Ma, Q. Liu, W. Ke, Z. Chen, L. Xiong, P. Qin, Z. Chen, M. Qin, X. Lu, Y. Yan, G. Fang, *Small* **2017**, *13*, 1601769.
[19] Z. Yu, L. Sun, *Small Methods* **2017**, *2*, 1700280.
[20] H. Zhang, J. Cheng, F. Lin, H. He, J. Mao, K. S. Wong, A. K. Y. Jen, W. C. H. Choy, *ACS Nano* **2016**, *10*, 1503.
[21] J.-Y. Jeng, K.-C. Chen, T.-Y. Chiang, P.-Y. Lin, T.-D. Tsai, Y.-C. Chang, T.-F. Guo, P. Chen, T.-C. Wen, Y.-J. Hsu, *Adv. Mater.* **2014**, *26*, 4107.
[22] X. Yin, M. Que, Y. Xing, W. Que, *J. Mater. Chem. A* **2015**, *3*, 24495.
[23] L. Xu, X. Chen, J. Jin, W. Liu, B. Dong, X. Bai, H. Song, P. Reiss, *Nano Energy* **2019**, *63*, 103860.
[24] Y. Liu, J. Duan, J. Zhang, S. Huang, W. Ou-Yang, Q. Bao, Z. Sun, X. Chen, *ACS Appl. Mater. Interfaces* **2020**, *12*, 771.
[25] K.-C. Wang, J.-Y. Jeng, P.-S. Shen, Y.-C. Chang, E. W.-G. Diau, C.-H. Tsai, T.-Y. Chao, H.-C. Hsu, P.-Y. Lin, P. Chen, T.-F. Gao, T.-C. Wen, *Sci. Rep.* **2014**, *4*, 4756.
[26] K.-C. Wang, P.-S. Shen, M.-H. Li, S. Chen, M.-W. Lin, P. Chen, T.-F. Guo, *ACS Appl. Mater. Interfaces* **2014**, *6*, 11851.
[27] Y. Guo, X. Yin, W. Que, *J. Alloys Compd.* **2017**, *722*, 839.
[28] K. Yao, F. Li, Q. He, X. Wang, Y. Jiang, H. Huang, A. K.-Y. Jen, *Nano Energy* **2017**, *40*, 155.
[29] J. Sun, J. Lu, B. Li, L. Jiang, A. S. R. Chesman, A. D. Scully, T. R. Gengenbach, Y.-B. Cheng, J. J. Jasieniak, *Nano Energy* **2018**, *49*, 163.
[30] X. Yin, J. Zhai, P. Du, N. Li, L. Song, J. Xiong, F. Ko, *ChemSusChem* **2020**, *13*, 1006.
[31] T. Sreethawong, S. Chavadej, S. Ngamsinlapasathian, S. Yoshikawa, *Colloids Surf., A* **2007**, *296*, 222.
[32] L. Li, E. A. Gibson, P. Qin, G. Boschloo, M. Gorlov, A. Hagfeldt, L. Sun, *Adv. Mater.* **2010**, *22*, 1759.
[33] R. Keshavarzi, V. Mirkhani, M. Moghadam, S. Tangestaninejad, I. Mohammadpoor-Baltork, *Langmuir* **2015**, *31*, 11659.

[34] M. Templin, A. Franck, A. Du Chesne, H. Leist, Y. Zhang, R. Ulrich, V. Schädler, U. Wiesner, *Science* **1997**, *278*, 1795.
[35] M. Amini, R. Keshavarzi, V. Mirkhani, M. Moghadam, S. Tangestaninejad, I. Mohammadpoor-Baltork, F. Sadegh, *J. Mater. Chem. A* **2018**, *6*, 2632.
[36] J. de A. Rodrigues Jr., R. S. V. Nascimento, *J. Appl. Polym. Sci.* **2010**, *116*, 3047.
[37] P. S. Patil, L. D. Kadam, *Appl. Surf. Sci.* **2002**, *199*, 211.
[38] J. R. Manders, S.-W. Tsang, M. J. Hartel, T.-H. Lai, S. Chen, C. M. Amb, J. R. Reynolds, F. So, *Adv. Funct. Mater.* **2013**, *23*, 2993.
[39] J. H. Lee, Y. W. Noh, I. S. Jin, S. H. Park, J. W. Jung, *ACS Sustainable Chem. Eng.* **2019**, *7*, 15495.
[40] Z. Zhu, Y. Bai, T. Zhang, Z. Liu, X. Long, Z. Wei, Z. Wang, L. Zhang, J. Wang, F. Yan, S. Yang, *Angew. Chem., Int. Ed.* **2014**, *53*, 12571.
[41] C. J. Flynn, S. M. McCullough, E. Oh, L. Li, C. C. Mercado, B. H. Farnum, W. Li, C. L. Donley, W. You, A. J. Nozik, J. R. McBride, T. J. Meyer, Y. Kanai, J. F. Cahoon, *ACS Appl. Mater. Interfaces* **2016**, *8*, 4754.
[42] H.-S. Kim, J.-Y. Seo, H. Xie, M. Lira-Cantu, S. M. Zakeeruddin, M. Grätzel, A. Hagfeldt, *ACS Omega* **2017**, *2*, 9074.
[43] M. C. Fuertes, F. J. López-Alcaraz, M. C. Marchi, H. E. Troiani, V. Luca, H. Hernán Míguez, G. J. A. A. Soler-Illia, *Adv. Funct. Mater.* **2007**, *17*, 1247.
[44] Y. J. Kim, Y. H. Lee, M. H. Lee, H. J. Kim, J. H. Pan, G. Il Lim, Y. S. Choi, K. Kim, N.-G. Park, C. Lee, W. I. Lee, *Langmuir* **2008**, *24*, 13225.
[45] A. B. Kunz, *J. Phys. C: Solid State Phys.* **1981**, *14*, L455.
[46] P. Kaienburg, P. Hartnagel, B. E. Pieters, J. Yu, D. Grabowski, Z. Liu, J. Haddad, U. Rau, T. Kirchartz, *J. Phys. Chem. C* **2018**, *122*, 27263.
[47] W. Zhang, M. Saliba, D. T. Moore, S. K. Pathak, M. T. Hörantner, T. Stergiopoulos, S. D. Stranks, G. E. Eperon, J. A. Alexander-Webber, A. Abate, A. Sadhanala, S. Yao, Y. Chen, R. H. Friend, L. A. Estroff, U. Wiesner, H. J. Snaith, *Nat. Commun.* **2015**, *6*, 6142.
[48] Q. Lian, M. Z. Mokhtar, D. Lu, M. Zhu, J. Jacobs, A. B. Foster, A. G. Thomas, B. F. Spencer, S. Wu, C. Liu, N. W. Hodson, B. Smith, A. Alkaltham, O. M. Alkhudhari, T. Watson, B. R. Saunders, *ACS Appl. Mater. Interfaces* **2020**, *12*, 18578.
[49] D. Yang, L. Zhou, W. Yu, J. Zhang, C. Li, *Adv. Energy Mater.* **2014**, *4*, 140059.
[50] D. Yang, R. Yang, K. Wang, C. Wu, X. Zhu, J. Feng, X. Ren, G. Fang, S. Priya, S. (Frank) Liu, *Nat. Commun.* **2018**, *9*, 3239.
[51] Y. Li, L. Ji, R. Liu, C. Zhang, C. H. Mak, X. Zou, H.-H. Shen, S.-Y. Leu, H.-Y. Hsu, *J. Mater. Chem. A* **2018**, *6*, 12842.
[52] Y. Liu, S. Akin, A. Hinderhofer, F. T. Eickemeyer, H. Zhu, J.-Y. Seo, J. Zhang, F. Schreiber, H. Zhang, S. M. Zakeeruddin, A. Hagfeldt, M. I. Dar, M. Grätzel, *Angew. Chem., Int. Ed.* **2020**, *59*, 15688.
[53] H.-S. Kim, J.-Y. Seo, S. Akin, E. Simon, M. Fleischer, S. M. Zakeeruddin, M. Grätzel, A. Hagfeldt, *Nano Energy* **2019**, *61*, 126.
[54] Y. Shao, Y. Fang, T. Li, Q. Wang, Q. Dong, Y. Deng, Y. Yuan, H. Wei, M. Wang, A. Gruverman, J. Shield, J. Huang, *Energy Environ. Sci.* **2016**, *9*, 1752.
[55] P. Calado, A. M. Telford, D. Bryant, X. Li, J. Nelson, B. C. O'Regan, P. R. F. Barnes, *Nat. Commun.* **2016**, *7*, 13831.
[56] J.-P. Correa-Baena, M. Anaya, G. Lozano, W. Tress, K. Domanski, M. Saliba, T. Matsui, T. J. Jacobsson, M. E. Calvo, A. Abate, M. Grätzel, H. Míguez, A. Hagfeldt, *Adv. Mater.* **2016**, *28*, 5031.
[57] S. Akin, *ACS Appl. Mater. Interfaces* **2019**, *11*, 39998.
[58] W. Tress, M. Yavari, K. Domanski, P. Yadav, B. Niesen, J. P. Correa Baena, A. Hagfeldt, M. Graetzel, *Energy Environ. Sci.* **2018**, *11*, 151.
[59] M. Anaya, W. Zhang, B. C. Hames, Y. Li, F. Fabregat-Santiago, M. E. Calvo, H. J. Snaith, H. Míguez, I. Mora-Seró, *J. Mater. Chem. C* **2017**, *5*, 634.
[60] C. M. Wolff, P. Caprioglio, M. Stolterfoht, D. Neher, *Adv. Mater.* **2019**, *31*, 1902762.
[61] R. Wang, M. Mujahid, Y. Duan, Z.-K. Wang, J. Xue, Y. Yang, *Adv. Funct. Mater.* **2019**, *29*, 1808843.
[62] W. Nie, H. Tsai, R. Asadpour, J.-C. Blancon, A. J. Neukirch, G. Gupta, J. J. Crochet, M. Chhowalla, S. Tretiak, M. A. Alam, H.-L. Wang, A. D. Mohite, *Science* **2015**, *347*, 522.